frontiers | Frontiers in Earth Science

TYPE Original Research
PUBLISHED 16 January 2023
DOI 10.3389/feart.2022.1055957

OPEN ACCESS

EDITED BY
Tianchen He,
University of Leeds, United Kingdom

REVIEWED BY
Xiugen Fu,
Southwest Petroleum University, China
Santanu Banerjee,
Indian Institute of Technology Bombay, India

*CORRESPONDENCE
Kaibo Han,
hankb@cugb.edu.cn
Zhongpeng Han,
hanzp@cugb.edu.cn

SPECIALTY SECTION
This article was submitted to Biogeoscience, a section of the journal Frontiers in Earth Science

RECEIVED 28 September 2022
ACCEPTED 31 October 2022
PUBLISHED 16 January 2023

CITATION
Han K, Han Z, Garzanti E, Zhu S, Yao H, Guo H, Liu X and Wang C (2023), Middle Jurassic ooidal ironstones (southern Tibet): Formation processes and implications for the paleoceanography of eastern Neo-Tethys.
Front. Earth Sci. 10:1055957.
doi: 10.3389/feart.2022.1055957

Middle Jurassic ooidal ironstones (southern Tibet): Formation processes and implications for the paleoceanography of eastern Neo-Tethys

Kaibo Han[1,2]*, Zhongpeng Han[1,3]*, Eduardo Garzanti[4], Shuaipeng Zhu[1,3], Hanwei Yao[1,2], Huifang Guo[1,2], Xuan Liu[1,2] and Chengshan Wang[1,2]

[1]State Key Laboratory of Biogeology and Environmental Geology, China University of Geosciences, Beijing, China, [2]School of Earth Sciences and Resources, China University of Geosciences, Beijing, China, [3]Institute of Earth Sciences, China University of Geosciences, Beijing, China, [4]Department of Earth and Environmental Sciences, Università di Milano-Bicocca, Milano, Italy

The major facies changes documented in shallow-marine sediments of the northern Indian passive margin of Neo-Tethys throughout the Jurassic, from widespread platform carbonates in the Early Jurassic to organic-rich black shales in the Late Jurassic, imply a substantial turnover in oceanic conditions. All along the Tethys (Tibetan) Himalaya, from the Zanskar Range to southern Tibet, a peculiar interval characterized by ooidal ironstones of Dingjie Formation (Ferruginous Oolite Formation, FOF) marks the base of the organic-rich Spiti Shale. This laterally-extensive ooidal ironstone interval is a fundamental testimony of the mechanisms that led to major paleoceanographic changes that occurred in the eastern Neo-Tethys during the Middle Jurassic. In this article, we illustrate in detail the petrology, mineralogy, and geochemistry of ooidal ironstones and the major element contents of the entire Lanongla section. The FOF is characterized by significantly high contents of Fe_2O_3 (56.80% $\pm$ 9.07%, n = 7) and P_2O_5 (1.72% $\pm$ 1.19%, n = 7). In contrast, the Fe_2O_3 and P_2O_5 contents average 3.58% and 0.15% in the overlain carbonates of Lanongla Fm., and 5.55% and 0.16% in the overlying Spiti Shale. The ooidal ironstones are mainly composed of iron ooids with a few quartz grains and bioclasts cemented by sparry calcite. The iron ooids consist of concentric dark layers of francolite (carbonate fluorapatite), hence enriched in Ca, P, and F, and bright layers of chamosite, enriched in Fe, Si, Al, and Mg. Precipitation of francolite ensued from oversaturation of phosphorous ascribed to intensified upwelling, high biogenous productivity, and degradation of organic matter, whereas the formation of chamosite reflects enhanced continental weathering and erosion leading to increased Fe input to the ocean during transgressive stages characterized by low sedimentation rate and scarce oxygenation at the seafloor. Modern upwelling zones in outer shelf or slope areas perform similar geochemical characteristics to those as observed in this study. Under the Mesozoic greenhouse background, fluctuating redox conditions induced the alternate growth of francolite under anoxic conditions and of chamosite under

suboxic conditions. Ooids were thus formed on the seafloor during continued resuspension and vertical oscillations of the chemocline rather than from interstitial waters after burial. The mineralogy of iron ooids indicates mainly reducing conditions in the water column, suggesting that extensive upwelling along the continental margin of eastern Neo-Tethys contributed significantly to the transition from carbonate deposits to organic-rich black shales during the Jurassic, as testified by the transition from well-oxygenated in Lanongla Fm. To a reduceing condition in Spiti Shale indicated by the Mn/Al ratios compared to PAAS.

KEYWORDS

ooidal ironstone, facies changes, fluctuating redox conditions, upwelling, southern Tibet

Introduction

Ooidal ironstones represent a unique sediment type where ooid content exceeds 5% in volume and Fe content is >15 wt% (21.4 wt% Fe_2O_3) (Young, 1989; Vanhouten, 1992; Salama et al., 2012). In exceptional cases, the abundance of ferruginous ooids may be much higher than 5% (Burkhalter, 1995) and even exceed 50% (McGregor et al., 2009). These peculiar sediments are mainly deposited in marine environments (Vanhouten, 1985, 1992; Young, 1989, 1992), but were locally reported from Jurassic to Neogene non-marine strata (McGregor et al., 2009). Ferruginous ooids are distinguished from more common carbonate ooids by their high iron content and generally concentric fabric (radial fabric has been reported so far only from Jurassic ironstones in Iran; Rahiminejad and Zand-Moghadam, 2018). The main iron-rich minerals include hematite, goethite, and chamosite (Mucke and Farshad, 2005).

The ooidal ironstones record the redox states and chemical conditions of the ocean and atmosphere (Sturesson, 1992, 2003), and reflect the evolution of tectonic, magmatic, and biological activities (Garzanti et al., 1989; Vancappellen and Berner, 1991; Garzanti, 1993; Follmi, 1996, 2016; Tang et al., 2017; Rahiminejad and Zand-Moghadam, 2018; Rudmin et al., 2020). Deposition of marine ooidal ironstones took place preferentially during periods of rapid transgression leading to condensed deposition (Vanhouten and Purucker, 1984; Garzanti et al., 1989; Vanhouten, 1992; Donaldson et al., 1999; Sturesson, 2003; Taylor and Macquaker, 2011; Follmi, 2016).

Ooidal ironstones are temporally distributed from the Precambrian to the present day (Young, 1989; Mucke and Farshad, 2005), and were principally reported to occur in the Ordovician to Devonian and in the Jurassic to Paleogene (Rahiminejad and Zand-Moghadam, 2018). Jurassic ooidal ironstones are widely developed in Asia, Europe, and Oceania. In the Indian passive margin of eastern Neo-Tethys, ooidal ironstones extensively occur in the Bajocian-Callovian, and are traced from the Zanskar Range to central Nepal and southern Tibet as marker beds for stratigraphic correlation (Garzanti et al., 1989; Jadoul et al., 1998). These Middle Jurassic ironstones, named as Ferruginous Oolite Formation (FOF) all along the Tethys (Tibetan) Himalaya (Garzanti, 1993, 1999; Sciunnach and Garzanti, 2012), are also termed Dingjie Formation in southern Tibet (Li and Wang, 2005). Garzanti et al. (1989) suggested that the ooidal ironstones of the Tibetan Himalaya were deposited in high-energy environments during a stage of starved sedimentation induced by rapid transgression.

The Jurassic shallow-marine sedimentary succession deposited along the southeastern margin of Neo-Tethys documents a radical change from Lower Jurassic platform carbonates (Kioto Group) to Upper Jurassic organic-rich black mudstones (Spiti Shale) (Dera et al., 2011). This change was realized stepwise between the Toarcian, when the first oceanic anoxic event was recorded (Jadoul et al., 1998), and the Upper Jurassic Spiti Shale. The demise of the carbonate platform took place during an interval characterized by global warming and pulses of rapid transgression through the late Middle Jurassic (Dera et al., 2011), as testified by the Ferruginous Oolite Formation. Investigating the sedimentary processes that lead to the deposition of this peculiar stratigraphic unit is essential to better understand the paleoclimatic and paleoceanographic evolution of eastern Neo-Tethys in this crucial period time. To reach this goal, and provide new insights into the chemical and physical conditions that led to the extensive formation of ooidal ironstones, we studied in detail the mineralogy, chemistry, and structure of these ferruginous ooids contained in the Middle Jurassic Ferruginous Oolite Formation exposed in southern Tibet and discuss their formation process. Major elements contents of bulk rocks were measured in order to explore the chemical compositions and the redox condition changes in the south Tethys margin of the Middle Jurassic.

Geological setting

The Tethys Himalayan Zone in southern Tibet is bounded to the north by the Yarlung Zangpo suture zone, including the Xigaze Forearc Basin floored by the Yalung-Zangbo Ophiolite,

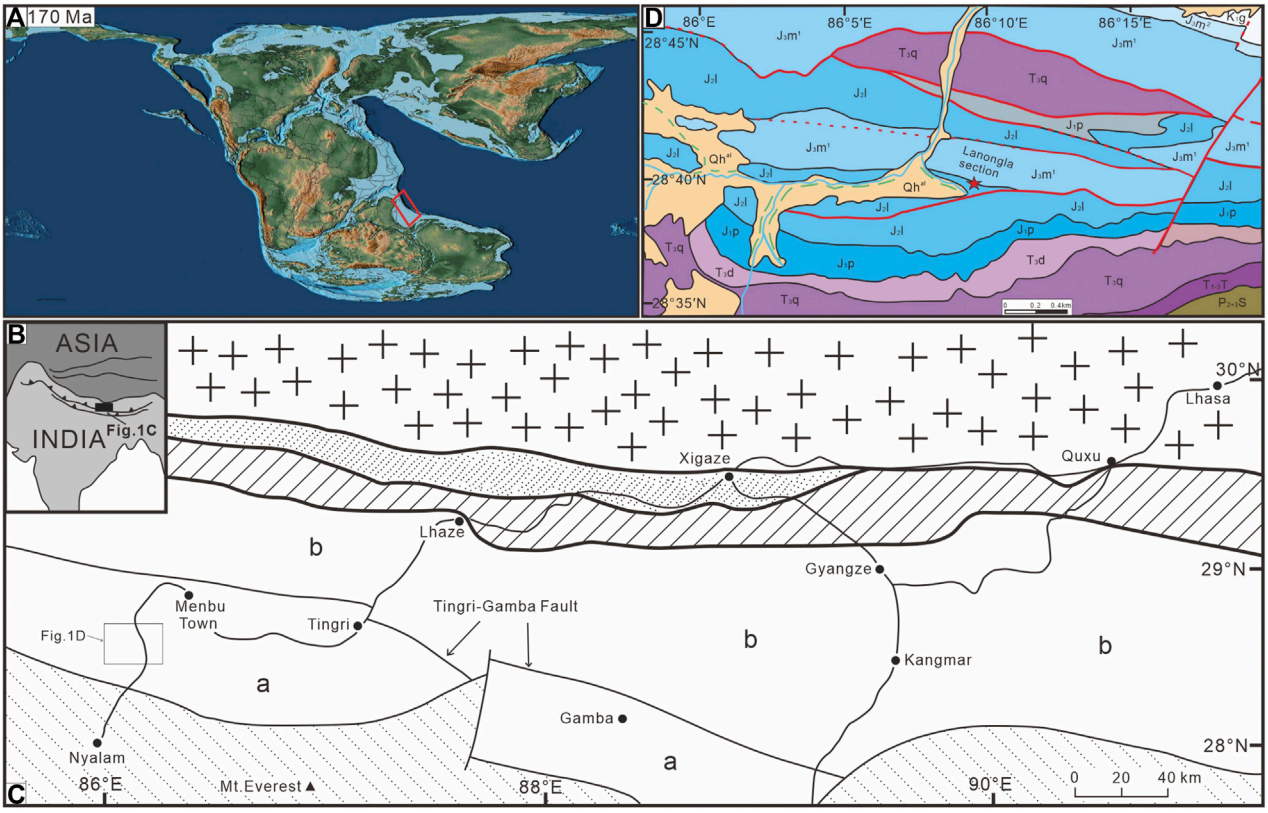

FIGURE 1
The study area in southern Tibet. **(A)** Global paleogeographic map for the Bajocian-Bathonian (~170 Ma; after Scoteses, 2014); red rectangle shows location of Tethys Himalaya; **(B,C)** Tectonic map of southern Tibet (adapted from Li et al., 2006); **(D)** Geological map of the studied area (red star indicates location of the studied Lanongla section).

and it is separated from metamorphic rocks of the Greater Himalaya by the South Tibetan Detachment in the south Figures 1B,C. In the Middle Jurassic, the Tethys Himalaya was part of the passive continental margin of northern India facing the Neo-Tethys Ocean and located at middle-low latitudes of the southern Hemisphere (red rectangle in Figure 1A). The Tethys Himalaya is traditionally subdivided into northern and southern subzones (Figure 1C) (Wang et al., 2005). Our study area near the Nyalam County is part of the southern subzone, where mainly shallow-marine sediments were deposited in the Mesozoic (Figure 1D). The Jurassic sedimentary succession includes medium-bedded oolitic limestones and sandstones of the Lower Jurassic Pupuga Formation (local name of the lower Kioto Group exposed throughout the Tethys Himalaya), representing a tidal flat sedimentary environment (Liu and Einsele, 1994; Shi et al., 1995; Jadoul et al., 1998), thin-bedded micritic limestones intercalated with occasional thin-bedded sandstones of the Nieniehsongla Formation (local name of the upper Kioto Group), representing a seaward sedimentary environment of carbonate ramp (Liu et al., 1983; Li and Grant-Mackie, 1993; Shi et al., 1995), marl and marly limestone couplets deposit of the Lalongla Formation, representing carbonate platform environment (Shi et al., 1995), the Dingjie Formation (Ferruginous Oolite Formation, proposed by Jadoul et al., 1998), and organic-rich black mudrocks of the Spiti Shale (member 1 of the Menkadun Fm.). The Jurassic succession of southern Tibet correlates well with equivalent stratigraphic units well exposed in Nepal and as far as the Zanskar-Spiti Synclinorium in the western Himalaya (Jadoul et al., 1998).

The age of the Pupuga Fm is constrained as Sinemurian to Pliensbachian by foraminiferal biostratigraphy (Han et al., 2021). The Nieniehsongla Fm. Is dated as Toarcian to Aalenian in age (Han et al., 2016 and references therein), the FOF as Bajocian to Callovian, and the Spiti Shale as Upper Jurassic (Yin, 2010). The FOF is well exposed in the studied Lanongla section of the Nyalam area (GPS: 28°29′56″N,87°06′32″E) (Figure 1D), being one of the five sections where iron oolites were previously studied in the same valley and in the Menbu area (Figure 1C) (Yin, 2010).

Materials and methods

Fresh samples were collected from the FOF of the Lanongla Section for this study and selected for the preparation of petrographic thin sections for microscope observations and of probe sections for morphological observations, and were carefully grounded (~200 mesh, in an agate mortar to avoid contamination) for X-Ray Diffraction (XRD) analysis. Petrographic analysis on thin sections using a Nikon-LV100POL polarizing microscope and cathodoluminescence (CL) observations were carried out at the China University of Geosciences (Beijing). Morphological observations of the microstructure of iron ooids and the measure of element concentrations on micrometer-sized spots were conducted at the State Key Laboratory of Biogeology and Environmental Geology, China University of Geosciences (Beijing), by a field emission scanning electron microscopy (SEM) using a ZEISS Supra 55 SEM equipped with an Oxford Electrical Refrigeration Energy Dispersive Spectrometer (EDS) operated at 20 kV with a working distance of 15 mm, specimen current of 200 nA, and beam diameter of ~1 mm. Before SEM examination and analyses, samples were coated with a ~10 nm thick platinum layer for electric conduction.

XRD analyses were carried out by Smart Lab of Japanese Technology Company in the laboratory of China University of Geosciences (Beijing) operated at 40 kV, 100 mA, scanning speed 8°per minute for phase and 2/4° per minute for crystal cells. The quantitative content analysis of mineral phases is based on the RIR (reference intensity ratio) calculation method proposed by ICDD (the International Centre for Diffraction Data), the relative standard deviation (RSD) is less than 5%.

At the State Key Laboratory of Biogeology and Environmental Geology, China University of Geosciences (Wuhan), Raman micro-spectroscopy was applied to further confirm the composition and distribution of different minerals within iron ooids. We used a WITec α 300 Confocal Raman system coupled with a Peltier cooled EMCCD detector, laser excitation at 532 nm with output power between 3 and 10 mW. Spectra were obtained using a 100× objective (N.A. = 0.9) with a 50 μm diameter optic fiber, grating 600 g/mm, obtaining a spectral resolution of ~4 cm^{-1}.

Twenty-two samples were selected and prepared to be analyzed for quantitative analyses of major elements content of bulk rock. This analysis was conducted by using a Shimadzu's wavelength dispersive X-ray fluorescence spectrometer (XRF) at the Ore Deposit Geochemistry Microanalysis Laboratory, affiliated with the State Key Laboratory of Geological Processes and Mineral Resources, China University of Geosciences, Beijing. Fused beads method was used in the preparation of test specimens. Mix weighed amounts of sample and flux and place the mixture in a clean platinum/gold crucible. In this study, a 0.7 g of sample (200 mesh) plus 7.0 g of mixed lithium borate fluxes were used. The addition of a small amount (100 mg) of a halide such as LiBr, acted as release agent when using platinum/gold molds. The mixture was heated in a high-frequency fusion machine at a fixed temperature, usually from 950 to 1100°C, until thoroughly melted. Fusion time was about 30 min. Then the fused beads were loaded into the XRF instrument for determination. Quantitative analyses of major elements were performed by the calibration curve method, the relative standard deviation (RSD) is less than 2%.

Results

Lithostratigraphy

In the Lanongla section, we measured and described in detail a 50 m-thick stratigraphic log across the FOF, starting from the middle part of the Lalongla Fm. And ending in the Spiti Shale. The Lalongla Fm. Here consists of marl and marly-limestone couplets with a few medium-bedded bioclastic limestones yielding abundant ammonites (*Chondroceras evolvescense* (Waagen), *Chondroceras cf. Crassicostatum* Westermann, *Dorsetensia cf. edouardiana and Stephanoceras* sp.), indicating an early Bajocian age (*Humphriesianum* Zone; Yin, 2010).

The FOF spans from ~22.5 to 27 m from the base of the section (Figure 2) and is characterized by reddish to yellow colors in the outcrop due to disseminated and weathered iron stain (Figure 3A). The basal contact with the Lalongla Fm. Is an erosive base (Figure 3B) and two units can be identified inside the FOF based on bioclastic content.

The 1.4 m-thick Unit A consists of medium-bedded ironstones with abundant fossils including corals, bivalves, foraminifera, and echinoderms (Figures 2, 3B). Abundant belemnites arranged parallel to the bedding surface occur at 1 m from the base (Figures 2, 3C) and a layer rich at ~1.3 m from the base (Figures 2, 3D) yielded abundant ammonites [*Phylloceras* sp., *Oxycerites cf. orbis* (Giebel), *Cadomites* sp., *Procerites* sp., *Macrocephalites gucuoi* (Westermann and Wang), *Macrocephalites cf. jaquoti* (Douvillé), *Choffatia* (*Grossouvria*) *cf. bathonica* (Mangold); Yin, 2010] indicating a late Bathonian age (Orbis Zone). The 2.6 m-thick Unit B, brown on weathered surface, consists of ironstones with abundant green ferruginous ooids and fine quartz grains set in dark brown ferruginous matrix. Fossil remains are few.

The overlying Spiti (Menkadun) black shales contain abundant ammonites of *Macrocephalites cf. jacquoti* (Douvillé), while *Homoeoplanulites cf. evolutum* Sandoval et Gabaron and *Homoeoplanulites balinensis* (Neumayr) indicate *Discus* zone of late Bathonian in west Europe, *Macrocephalites bifurcates, M. Gucuoi Jeanneticeras cf. Anomalum*, *Khaiceras cf. devauxi*, *Bomburites cf. microstoma* and *Neuqueniceras* (*Frickites*) *tibeticum* were found upward, which indicate an early Callovian age (Yin, 2010).

10.3389/feart.2022.1055957

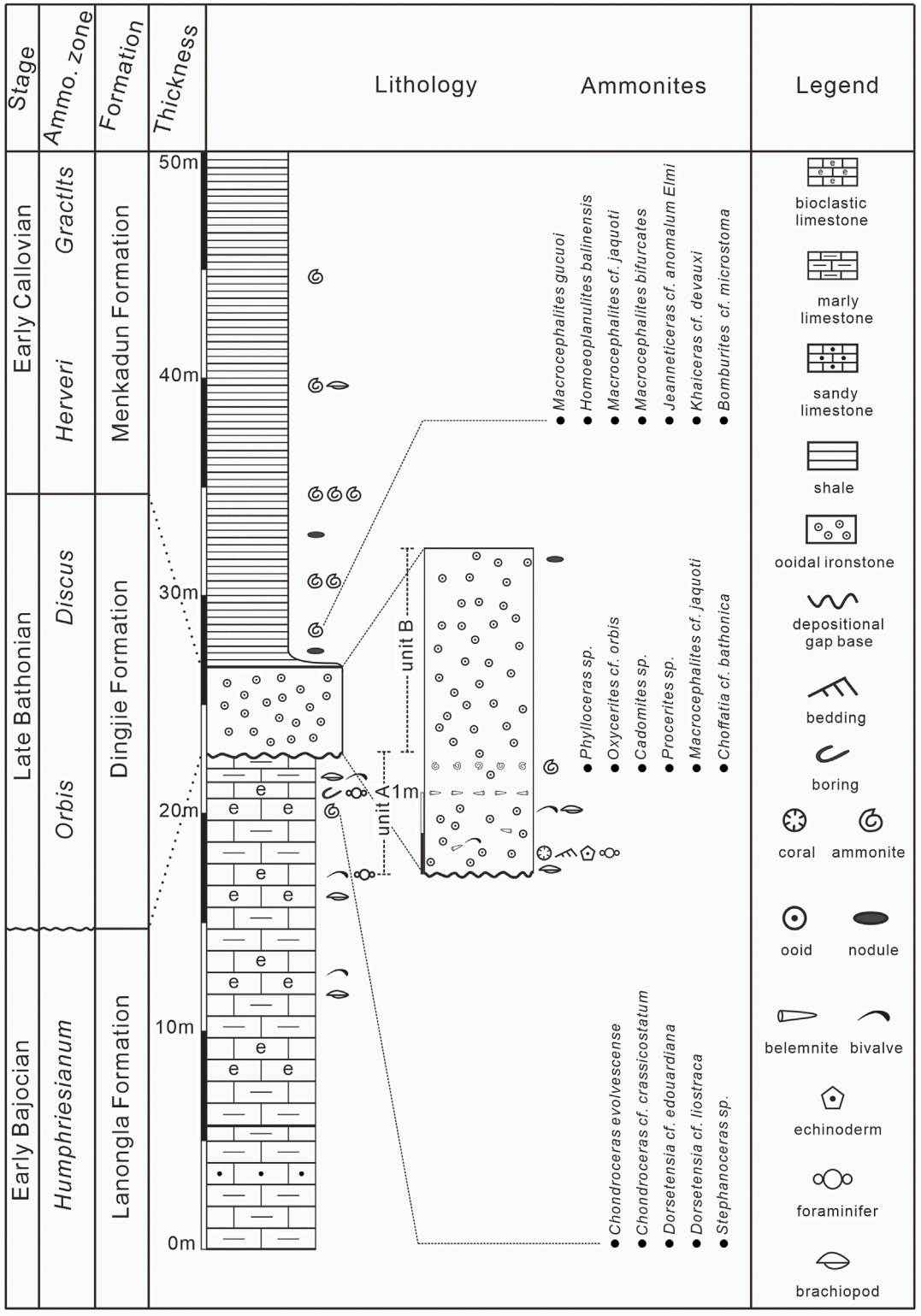

FIGURE 2
Middle Jurassic stratigraphy of the Lanongla Section with main fossil assemblages, ammonites and ammonite biostratigraphy are from Yin (2010).

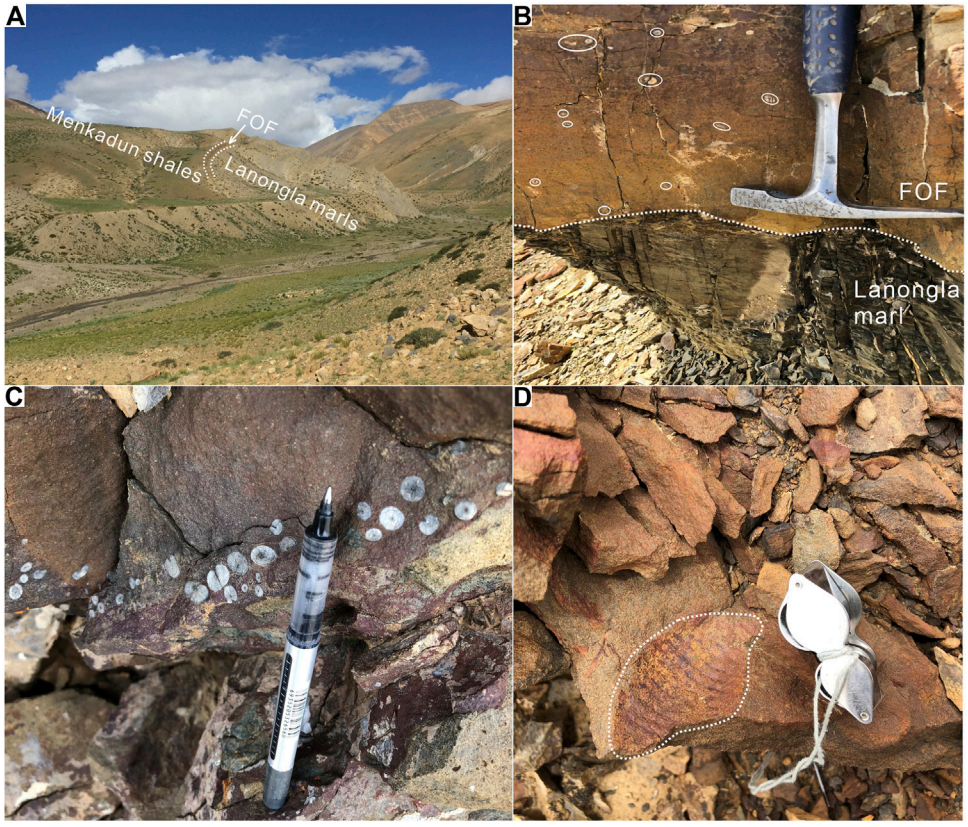

FIGURE 3
Ooidal ironstones of the Dingjie Fm (FOF). **(A)** Outcrop photograph, white dashed lines are the contacts of FOF with underlying Lanongla Fm. And overlying Spiti Shale. **(B)** Disconformable basal contact with the Lalongla Fm.; white ellipses encircle bioclasts. **(C)** Belemnite-rich layer in unit **(A)**. **(D)** Ammonite at the top of unit **(A)**.

According to ammonite biostratigraphy in Yin (2010), the FOF in this area represents the late Bathonian to early Callovian, and the basal disconformity with the Lalongla Fm. Testifies to a major stratigraphic hiatus of 8–10 Ma (Garzanti et al., 1989; Yin et al., 2000).

Elemental geochemistry

Major element concentrations are shown in Table 1. The Spiti Shale contains high concentration of Al_2O_3, TiO_2, and SiO_2. In contrast, the Lalongla Fm. Is characterized by high concentrations of CaO and MnO. The Mn/Al ratios in Lalongla Fm. Average ~0.02, which is ~10 times higher than the values of Spiti Shale (Table 1). The most remarkable feature of the element distribution in the studied succession is the prominent peaks of Fe_2O_3 and P_2O_5 in the FOF (Figure 4). The Fe_2O_3 concentrations in FOF average 56.80% and range from 42.98% to 66.39%, which is ~10 times higher than them in Lalongla Fm. And Spiti shales. The P_2O_5 concentrations in FOF (1.72% ± 1.19%, n = 6) are also much higher than in Lalongla and Spiti shales, where the P_2O_5 concentrations average 0.15% and 0.16%, respectively. The average of Fe/Al and P/Al ratios of FOF are 6.50 and 0.13 (Table 1; Figure 4), indicating significant enrichment of Fe and P compared to the post Proterozoic Australia Average Shale (PAAS) values (0.44 for Fe/Al and 0.009 for P/Al, Taylor and Mclennan, 1985). However, the Fe/Al and P/Al ratios in Lalongla and Spiti Shales are similar to PAAS values.

Ironstone petrography

Ironstones are mainly composed of spheroidal-ellipsoidal iron ooids mainly ranging from 100 μm to 550 μm in diameter (75%–85%), quartz grains (5%–10%), and bioclasts (5%–10%) cemented by calcite or, in some ooids, set in ferruginous matrix. Ferruginous ooids consist of a nucleus made of a bioclast, quartz grain, or a previously broken ooid

TABLE 1 Major element composition of the Lanongla section.

Samples	Thick-ness(m)	SiO_2 (wt %)	TiO_2 (wt %)	Al_2O_3 (wt%)	TFe_2O_3 (wt%)	MnO (wt%)	MgO (wt%)	CaO (wt %)	Na_2O (wt%)	K_2O (wt %)	P_2O_5 (wt %)	Mn/ Al	Fe/ Al	P/Al
18MB039	3	21.04	0.32	7.42	2.86	0.06	1.49	66.21	0.00	0.62	0.08	0.0113	0.5098	0.0094
18MB042	6.5	20.79	0.33	5.88	3.24	0.05	1.43	67.48	0.02	0.60	0.10	0.0125	0.7289	0.0137
18MB044	8.5	12.11	0.16	5.17	4.53	0.07	1.54	75.59	0.35	0.28	0.31	0.0187	1.1588	0.0495
18MB045	10	15.85	0.25	4.53	3.36	0.06	1.46	73.66	0.05	0.50	0.05	0.0195	0.9813	0.0085
18MB047	15.8	15.16	0.22	5.88	2.46	0.09	1.79	73.80	0.20	0.39	0.14	0.0226	0.5530	0.0193
18MB048	19.3	14.37	0.22	6.33	3.40	0.07	1.58	73.47	0.00	0.40	0.25	0.0171	0.7099	0.0322
18MB050	21.8	14.90	0.24	7.38	5.23	0.08	2.06	68.87	0.45	0.47	0.11	0.0153	0.9374	0.0128
18MB053	23.3	16.57	0.35	10.79	48.32	0.10	2.58	17.32	0.11	0.02	3.55	0.0132	5.9213	0.2716
18MB055	24.3	16.48	0.48	10.34	59.86	0.11	2.91	7.82	0.01	0.12	1.92	0.0160	7.6494	0.1534
18MB056	25	14.50	0.47	10.29	62.15	0.07	2.15	8.23	0.00	0.03	2.18	0.0106	7.9789	0.1746
18MB057	25.5	14.51	0.48	10.10	66.39	0.15	1.61	3.94	0.58	0.04	1.77	0.0220	8.6887	0.1448
18MB058	26	17.27	0.78	15.59	61.07	0.07	2.62	1.23	0.81	0.05	0.68	0.0062	5.1761	0.0362
18MB059	26.5	29.74	0.60	15.90	42.98	0.14	2.77	7.52	0.00	0.10	0.18	0.0125	3.5721	0.0093
18MB062	30	76.00	0.80	15.64	4.70	0.02	0.53	0.52	0.24	1.72	0.08	0.0015	0.3972	0.0043
18MB063	32	71.31	1.02	17.93	5.37	0.02	0.57	0.53	0.19	2.67	0.13	0.0014	0.3959	0.0058
18MB064	34	67.69	1.05	19.87	6.29	0.02	0.61	0.61	0.27	2.92	0.25	0.0014	0.4181	0.0104
18MB065	36	75.54	0.91	14.40	5.68	0.02	0.52	0.54	0.23	2.24	0.14	0.0023	0.5214	0.0080
18MB066	38	67.01	1.06	20.35	5.82	0.03	0.61	0.57	0.90	2.95	0.15	0.0019	0.3777	0.0059
18MB067	41	69.85	1.10	19.57	3.32	0.01	0.50	0.69	1.50	2.95	0.12	0.0004	0.2240	0.0050
18MB068	43	73.91	0.90	14.94	5.28	0.01	0.48	0.58	1.26	2.23	0.15	0.0014	0.4674	0.0083
18MB069	44.5	74.85	0.87	15.14	4.33	0.01	0.55	0.57	1.19	2.08	0.13	0.0008	0.3782	0.0071
18MB070	47	66.65	0.93	18.13	9.14	0.02	0.51	0.66	0.22	2.50	0.29	0.0012	0.6661	0.0132

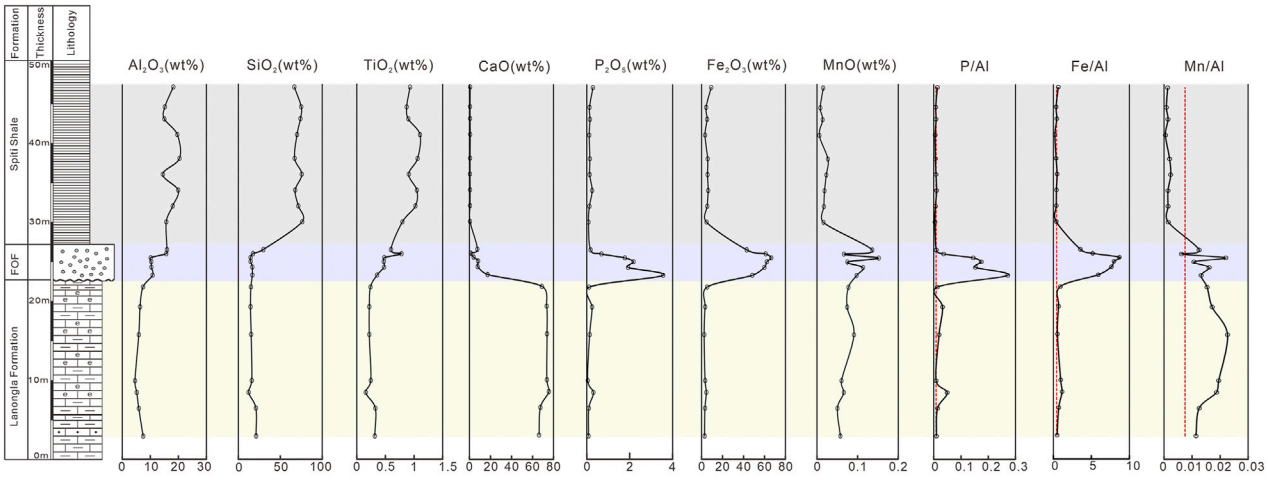

FIGURE 4
Major elements distribution along the profiled lithological column and the Al-normalized P, Fe, Mn contents and their reference lines of PAAS (red dashed lines). Clear segmentation can be seen in these three Formations according to the contents of the elements.

with a cortex of concentric layers (Figure 5A), and appear extinct at the microscope under cross polarized light (Figure 6A). Most ooids, whole or broken, are overgrown by brown ferruginous material that may also replace the ooid's nucleus (Figure 5B). Calcite cements display ferruginous stain especially adjacent to the ooids.

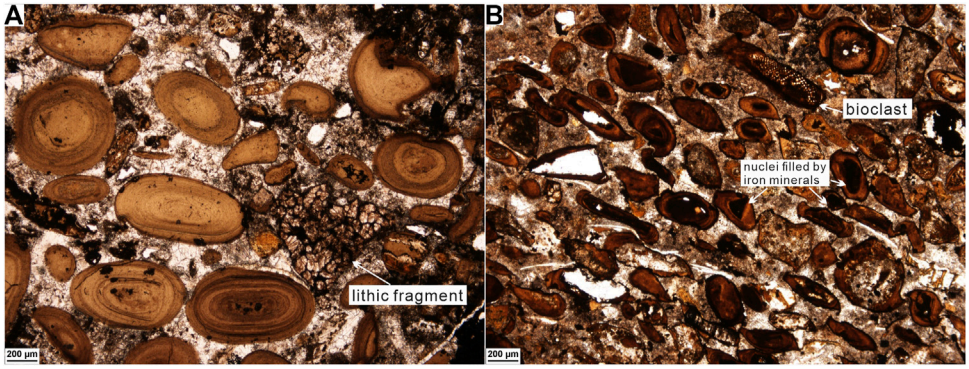

FIGURE 5
Morphological characteristics of FOF ironstones in thin sections under single polarized microscope. **(A)** Iron ooids showing concentric texture. **(B)** Deformed and broken iron ooids with nucleus commonly filled by ferruginous material and rare bioclasts.

Mineralogy of iron ooids

X-ray diffraction (XRD) analyses of bulk-rock powder exhibit the characteristic peaks of the chlorite group (d-spacing ~3.52, ~7.07, and ~14.2 nm), goethite (d-spacing ~4.17 and ~2.69 nm), and calcite (d-spacing ~3.03 nm) (Figure 6F). The estimated proportions of these minerals are ~60% calcite, ~10% chlorite group, ~5% goethite, the rest remaining undetermined (see below). The combination of optical, SEM, CL, and Raman analyses indicate that calcite is contained chiefly as cement, that ooids mostly consist of phyllosilicates, and that goethite is present as the principal mineral of ferruginous overgrowths on the edge of ooids and as stain of cement. Cross extinction of the ooids under the microscope, dark blue color in CL images, and high Fe content detected by SEM-EDS indicate that the phyllosilicate mineral of the chlorite group contained in ferruginous ooids is chamosite (or possibly berthierine, which may be transformed to chamosite during burial; Hornibrook and Longstaffe, 1996).

Raman analysis of iron ooids indicate the presence of organic matter (red areas in Figure 6C and spectrum with peaks at 1338 and 1604 cm^{-1} in Figure 6D) and apatite (jade-green areas in Figure 6C and spectrum with peaks at 964, 1337, and 1603 cm^{-1} in Figure 6D). Darker layers enriched in Ca, P, and F and colored in light blue in CL images (Figure 6B) thus consist of carbonate fluorapatite (francolite). Both francolite and organic matter were not detected by XRD analyses because of their fine structure and weak signal.

Chemistry of iron ooids

In SEM images, iron ooids appear zoned with alternating brighter and darker layers varying in width from a few μm to tens of μm (Figure 6E). The transition between layers is abrupt. EDS results on four points selected to assess the chemical composition of different layers show that brighter layers (points a and d in Figure 7) are enriched in Fe, Al, Si, and Mg—the typical composition of phyllosilicates, whereas darker layers (points b and c in Figure 7) are enriched in Ca, P, and F. The spatial distribution of chemical elements was further investigated in detail with continuous semi-quantitative EDS line-scan analyses from the center to the edge of two ooids with well-preserved concentric fabric (Figure 7). Results indicate an inverse correlation between Fe versus Ca and P, the former reaching minimum in darker layers and the latter minimum in brighter layers.

Discussion

Sources of iron and phosphorous

The formation of iron ooids, consisting of concentric layers of chamosite and francolite, require a sufficient supply of Fe and P into seawater of the eastern Tethys Ocean during the late Bathonian. Main sources of iron may be derived from submarine volcanism (Sturesson et al., 2000; Garcia-Frank et al., 2012), deep-sea hydrothermal fluids (Kimberley, 1994; Khadkikar, 1996), or terrestrial weathering and erosion (Berendsen et al., 1992; Andreeva and Chatalov, 2011). The concentration of iron occurs during periods of starved sedimentation (Li and Wang, 2005), and geochemical precipitation is generally associated with bacterial activity (Nelson et al., 2010).

Magmatic and hydrothermal supply could have hardly represented a major source of iron during the sedimentation of the FOF. At the global scale, major Jurassic magmatic events (e.g., Karoo-Ferrar large igneous province, Duncan et al., 1997; central Atlantic magmatic province, Knight et al., 2004; North Sea volcanism, Bergelin et al., 2011; Patagonia volcanism,

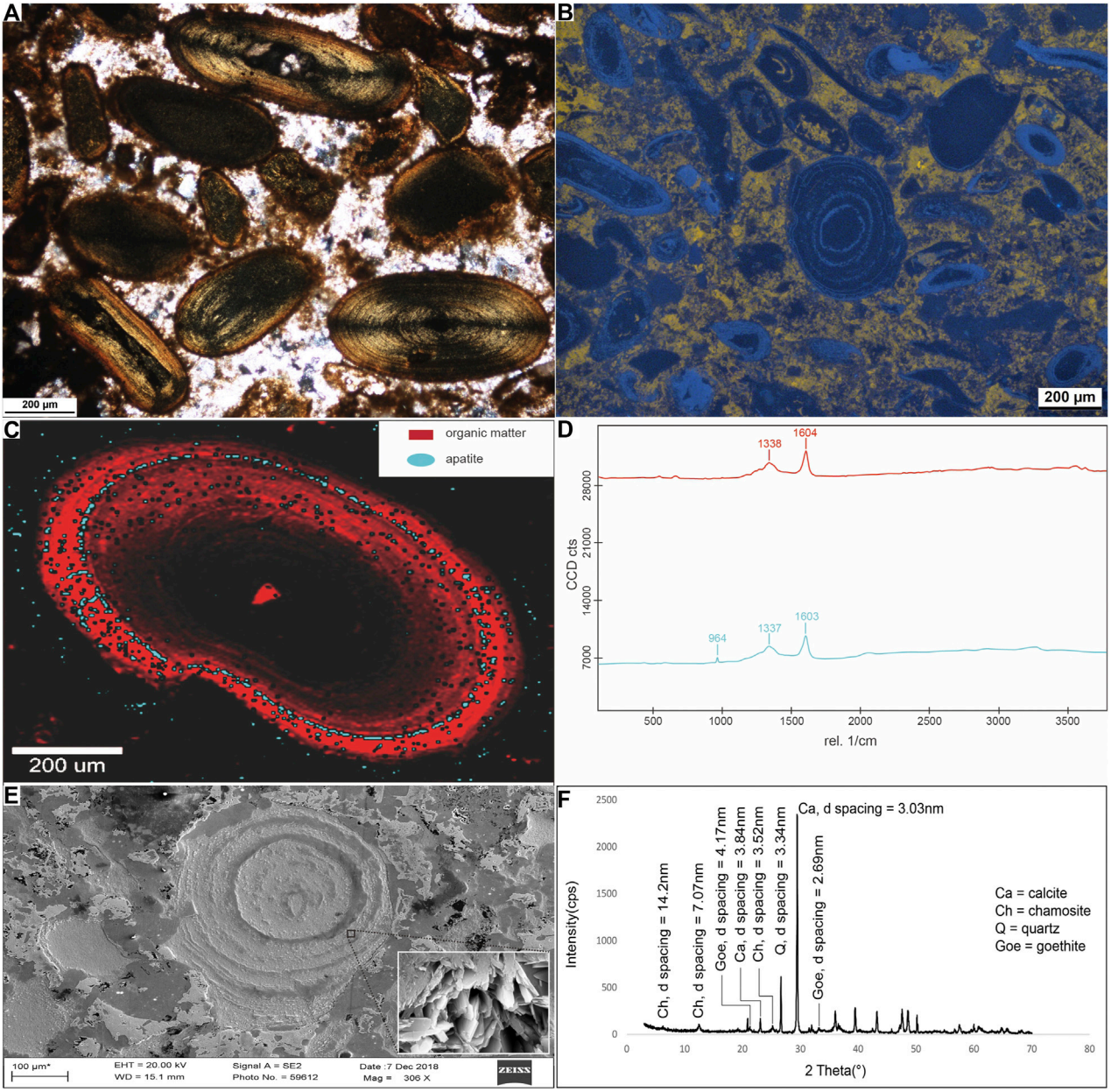

FIGURE 6
Optical, cathodoluminescence, SEM, Raman, and XRD analyses of iron ooids. **(A)** Iron ooids under cross-polarized light in thin section. **(B)** Concentric structure highlighted in blue colors under cathodoluminescence. **(C)** Raman spectroscopy image showing the distribution of organic matter and apatite with characteristic Raman spectra **(D)**. **(E)** Concentric structure highlighted under the scanning electron microscope with lamellar structure of brighter layers emphasized after magnification. **(F)** XRD bulk-rock analyses of ooidal ironstone.

Pankhurst et al., 1998) did not occur in the late Bathonian to early Callovian (Dera et al., 2011). At the regional scale, Middle Jurassic volcanism in surrounding areas is limited to local occurrence of basalt in deep-sea environments (Zhu et al., 2004).

As far as global paleoclimate is concerned, a rapid warming event took place in the late Bathonian although the Middle Jurassic was generally a cool period (e.g., Dera et al., 2011). Climatic warming enhances the intensity of continental weathering and the hydrological cycle, and consequently iron supply to the ocean. The concurrent substantial sea-level rise in the late Bathonian (Surlyk, 1991) may have resulted from melting of polar glaciers, resulting in starved sedimentation and reduced oxygenation in marginal seas (Handoh et al., 2003). The ooidal ironstones of the FOF mantled the underlying disconformity

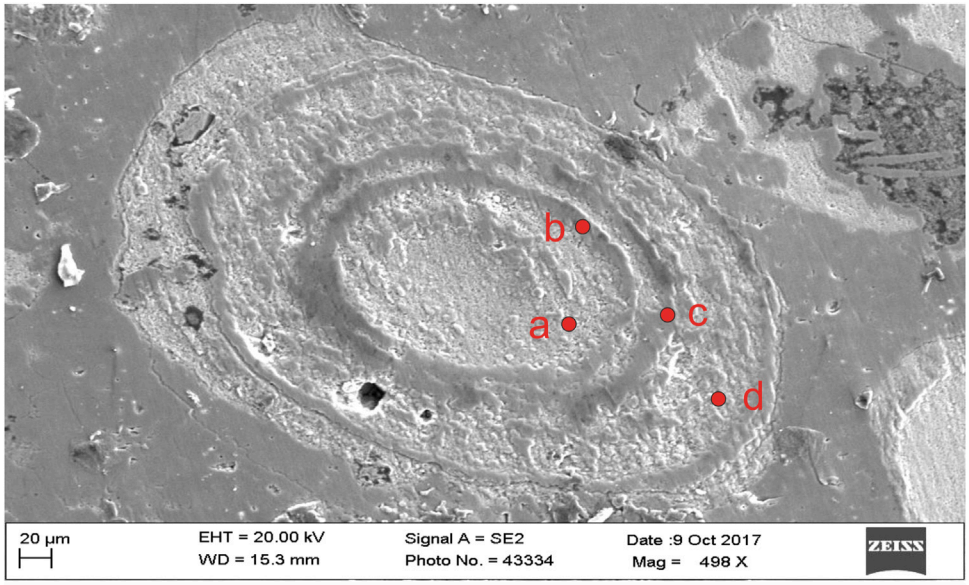

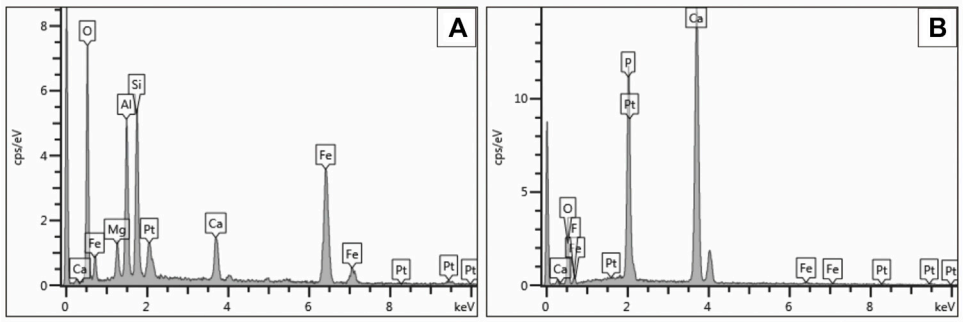

elements	O	Mg	Al	Si	Ca	P	Fe	F	total
wt%	46.17	2.78	10.07	10.53	3.89	0	26.57	0	100.00

elements	O	Mg	Al	Si	Ca	P	Fe	F	total
wt%	38.18	0	0	0	37.49	17.15	0.64	6.55	100.00

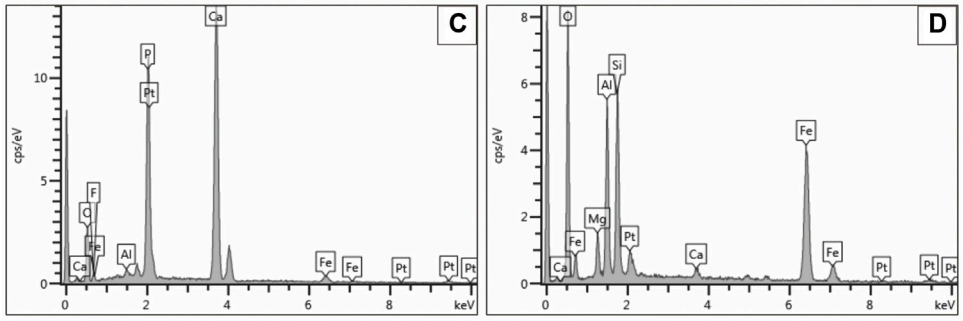

elements	O	Mg	Al	Si	Ca	P	Fe	F	total
wt%	42.33	0	0.58	0	34.02	16.22	2.05	4.80	100.00

elements	O	Mg	Al	Si	Ca	P	Fe	F	total
wt%	44.71	3.24	10.68	11.30	0.77	0	29.29	0	100.00

FIGURE 7
Scanning electron microscope analyses. The four panels below [labelled **(A)** to **(D)**] are the energy spectrum results of the four points in the figure above; mass percentage content for each element is indicated.

during the early transgressive stage (Jadoul et al., 1998), when enhanced continental weathering and erosion led to increased iron supply to the marginal seas of the eastern Tethys Ocean. Very low sedimentation rate and deoxygenation at the sea floor led to the formation of chamosite. Similar scenario occurred during Cretaceous time (Donaldson et al., 1999).

Increasing supply of phosphorous and oversaturation may have resulted from organic matter degradation and subsequent

release of P from biogenic phosphate (Krajewski et al., 1994; Arning et al., 2009a; Reinhard et al., 2017). When ambient water is under anoxic condition, P can also be released by the reduction of Fe-oxyhydroxides and enrichment of inorganic phosphate by absorption in the sediment (Heggie et al., 1990; Nelson et al., 2010). Formation of carbonate fluorapatite (francolite) associated with microbial activity is well documented in the modern and ancient sedimentary record (Rao and Nair, 1988; Soudry and Lewy, 1988; Krajewski et al., 1994, 2000; Schulz and Schulz, 2005; Soudry et al., 2006; Arning et al., 2009b). In iron ooids of the FOF, francolite occurs mainly associated with high organic-matter content (Figure 6C), suggesting that the remobilization of P from organic matter is responsible for its formation. Increased P supply to the surface ocean may have been fostered by coastal upwelling, a process inferred to have led to peaks of phosphorite deposition during Ordovician and Miocene icehouse stages (Follmi, 1993; Dunn et al., 2021) as well as Cretaceous greenhouse stages (Donaldson et al., 1999). Generally, Because P retention is promoted by oxic bottomwaters whereas organic P delivery to the sediment is enhanced by benthic oxygen deficiency. The P accumulation rates are highest under suboxic conditions, particularly under fluctuating redox conditions (Jarvis et al., 1994; Algeo and Ingall, 2007). While during the Mesozoic warmhouse, even hothouse and oceanic anoxic periods (e.g., the T-OAE, OAE2) the shallow water region of eastern Tethys was in oxic state (Bomou et al., 2013; Han et al., 2022), thus the extensive coastal upwelling along the eastern Tethys is speculated that led to the high P input and the oxygen-depleted condition of the shallow region and the P accumulation in the FOF of Dingjie Formation.

Formation of alternating chamosite and francolite layers in iron ooids

Chamosite is an authigenic clay containing both ferric and ferrous iron and formed by the partial reduction of Fe-oxyhydroxide (Nelson et al., 2010). Chamosite precipitates under suboxic condition close to the Fe-redox boundary, whereas the release of P occurs in the more extreme condition of SO_4^{2-} reduction. Francolite, the most common phosphate mineral grown in marine environments (Follmi, 1996; Wigley and Compton, 2007), forms in suboxic to anoxic condition near the sediment-water interface in both upwelling (Glenn and Arthur, 1988; Arning et al., 2009b) and non-upwelling conditions (including paralic and deltaic siliciclastic settings and continental margins with low sedimentation rate; Heggie et al., 1990; Ruttenberg and Berner, 1993). Carbonate fluorapatite precipitation may have also resulted from the dissolution of calcite by bacterial sulfate reduction.

The existence of chamosite and francolite only within iron ooids, and their lack in the matrix, indicates that chamosite and francolite formed in the water column rather than from pore waters. We thus infer that the shallow Tethys Himalayan sea was mainly in suboxic/ferruginous condition leading to chamosite formation, whereas benthic water was in anoxic condition leading to degradation of organic matter, the release of P, and precipitation of francolite. The formation of alternating concentric layers of chamosite and francolite is explained by the vertical oscillation of the chemocline between ferruginous and anoxic conditions (Figure 8).

Chamosite formed when the ooids were suspended above the chemocline, whereas francolite precipitated when the ooids lay below the chemocline. Processes of biochemical precipitation were dominant in the late Bathonian, during a transgressive stage of starved sediment supply and minimal dilution by terrigenous detritus and bioclasts.

Paleoceanographic implications

The widespread deposition of FOF ooidal ironstones in the southern Tethys Himalaya indicates suboxic to anoxic in shallow-water environments of the southeastern Neo-Tethys Ocean during the late Bathonian-early Callovian. As shown by the elemental distributions through the section (Figure 4), the higher values of Al-normalized Mn indicate a well-oxygenated condition during the deposition of the carbonates of Lanongla Fm. A substantial increase in the contents of Fe and P indicates a ferruginous water condition as well as high productivity during the formation of FOF, both are possibly linked to upwelling, by which iron and phosphorus and oxygen-depleted water were carried up to the shallow areas the eastern Tethys. The relatively high values of Al-normalized Mn within the FOF interval probably result from the isomorphism permutation of iron by manganese in chamosite and in calcitic cements due to their similar ion radius and crystal structures during diagenesis (Wang and Chen., 1984; Curtis et al., 1986). Given the well lateral correlation for several kilometers of the FOF, although not necessarily strictly synchronous, this pattern implies a widespread development of upwelling along the southern Tethyan margin (Bansal et al., 2021).

During most of the Phanerozoic, sea waters remained well-oxygenated, with short-lived regional and global oceanic anoxic events (Larson and Erba, 1999; Jenkyns, 2010). During oceanic anoxic events (e.g., in the Toarcian or late Early Cretaceous), even surface waters could have become dysoxic to anoxic owing to the expansion of the oxygen minimum zone (Ifrim et al., 2011). These events were causally linked to massive volcanic activity and outgassing in large igneous provinces, leading to the onset of greenhouse conditions, rapid warming, transgression, upwelling, and increased primary productivity (Garzanti, 1991, 1993; Larson, 1991). Oceanic anoxic events were not reported in the Middle Jurassic, when icehouse climate prevailed (Dera et al., 2011), although a decrease in the oxygen dissolved in surface waters may have been induced by upwelling of reduced deep water (Scholz, 2018).

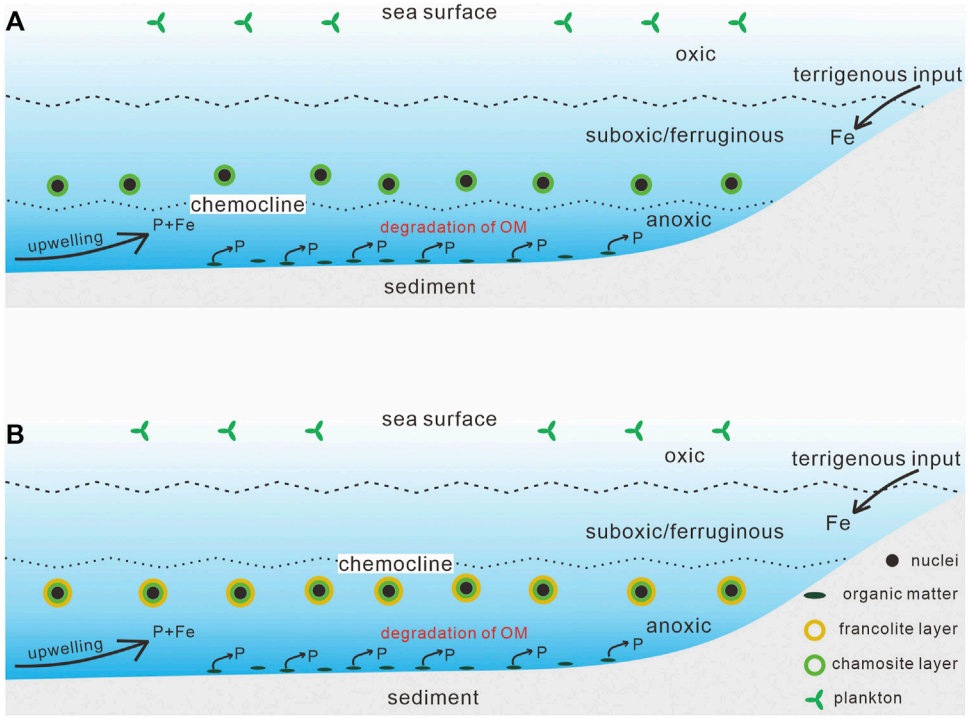

FIGURE 8
Processes leading to the formation of iron ooids in the FOF include intensified continental weathering and coastal upwelling that supplied Fe and P to the upper part of the water column. The ensuing increased productivity generated more organic matter that was degraded under anoxic conditions, thus releasing P again into anoxic waters. The vertical oscillation of the chemocline resulted in the formation of concentric chamosite and francolite layers: **(A)** chamosite formed in suboxic condition when the ooids lay above the chemocline; **(B)** francolite formed instead in anoxic condition when the ooids lay under the chemocline.

Tethys Himalayan sedimentation dramatically changed from marls and marly limestones to black shales in the late Middle Jurassic (Jadoul et al., 1998), when reducing condition in benthic waters (Wignall and Hallam, 1989; Jacobs and Lindberg, 1998) led to the burial of organic matter and subsequent positive $\delta^{13}C$ shift (Price and Grocke, 2002; Grocke et al., 2003).

Deoxygenation of surface waters is ascribed to coastal upwelling, increase in nutrients, and stimulated biogenous productivity in the photic zone. Degradation of organic matter released phosphorous into the water column, creating a positive feedback with anoxia that led to an elevated chemocline favoring the deposition of ooidal ironstones. Following the initial stage of rapid transgression, sedimentation rates increased terminating phosphate precipitation, whereas the formation of chamosite ceased when surface waters became more reducing than the suboxic state.

After the stage of widespread ironstone deposition testifying to extensive upwelling all along the Tethys Himalayan passive continental margin, strongly reducing conditions continued to develop indicated by the lower values of Mn/Al compared to PAAS, which led to the deposition of the Spiti Shale yielding a total organic carbon content (TOC) of ~1% (Li and Wang, 2005).

Evidence of sufficient Fe and P supply and regional reducing condition could be found in upwelling areas of outer shelf or slope of the modern sea, where chlorite and phosphorite often occur (Cook and Marshall, 1981; Arning et al., 2009a). The co-occurrence of organic-rich, phosphate and chamosite sediments of FOF and the organic-rich shales of Spiti Shale afterward as observed is consistent with those in modern upwelling zones (Glenn and Arthur, 1988; Glenn et al., 1994; Parrish et al., 2001; Banerjee et al., 2016).

Conclusion

The iron ooids contained in the Middle Jurassic Ferruginous Oolite Formation exposed in southern Tibet are composed of concentric dark layers of francolite (carbonate fluorapatite), hence enriched in Ca, P and F, and bright layers of chamosite enriched in Fe, Si, Al, and Mg. Precipitation of francolite ensued from oversaturation of P by intensified upwelling and degradation of organic matter, whereas the formation of chamosite reflects increased Fe input by enhanced continental weathering and erosion during a transgressive stage characterized by low sedimentation rate and scarce oxygenation at the sea floor.

Fluctuating redox conditions induced the alternate growth of francolite under anoxic conditions and of chamosite under suboxic conditions. Ooids were thus formed on the sea-floor during continued resuspension and vertical oscillations of the chemocline rather than from interstitial waters after burial.

The formation of iron ooids testifies to reducing conditions initiated in the Tethyan margins during the late Middle Jurassic. We suggest that extensive upwelling and more diffuse anoxia contributed to the demise of carbonate factories in the Tethyan domain since the late Early Jurassic under the Mesozoic greenhouse climatic conditions (Dera et al., 2011).

Data availability statement

The original contributions presented in the study are included in the article/supplementary material, further inquiries can be directed to the corresponding authors.

Author contributions

ZH, KH, and CW designed this study. KH, CW, and EG wrote the original manuscript. ZH instructed the field work and section measurement and analysis on the major elements. ZH helped with revising the manuscript. SZ, HY, HG, and XL contributed to sampling and testing.

Funding

This work is financially supported by NSFC projects (42072118, 41888101).

Acknowledgments

We are grateful to Jiao Liangxuan from the China University of Geosciences (Wuhan) for the help with the Raman test.

Conflict of interest

The authors declare that the research was conducted in the absence of any commercial or financial relationships that could be construed as a potential conflict of interest.

Publisher's note

References

Algeo, T. J., and Ingall, E. (2007). Sedimentary c_{org} : P ratios, paleocean ventilation, and phanerozoic atmospheric pO_2. *Palaeogeogr. Palaeoclimatol. Palaeoecol.* 256, 130–155. doi:10.1016/j.palaeo.2007.02.029

Andreeva, P., and Chatalov, A. (2011). Origin of the eifelian ironstones from well R-119 kardam, northeastern Bulgaria. *Comptes Rendus De. L Acad. Bulg. Des. Sci.* 64, 91–102.

Arning, E. T., Birgel, D., Brunner, B., and Peckmann, J. (2009a). Bacterial formation of phosphatic laminites off Peru. *Geobiology* 7, 295–307. doi:10.1111/j.1472-4669.2009.00197.x

Arning, E. T., Lueckge, A., Breuer, C., Gussone, N., Birgel, D., and Peckmann, J. (2009b). Genesis of phosphorite crusts off Peru. *Mar. Geol.* 262, 68–81. doi:10.1016/j.margeo.2009.03.006

Banerjee, S., Bansal, U., Pande, K., and Meena, S. S. (2016). Compositional variability of glauconites within the upper cretaceous karai shale formation, cauvery basin, India: Implications for evaluation of stratigraphic condensation. *Sediment. Geol.* 331, 12–29. doi:10.1016/j.sedgeo.2015.10.012

Bansal, U., Banerjee, S., Chauhan, G., Rudmin, M., Borgohain, D., and Upadhyay, A. (2021). "Geochemistry of Callovian ironstone in Kutch and its stratigraphic implications," in *Mesozoic stratigraphy of India - a multi-proxy approach*. Editors S. Banerjee and S. Sarkar (Springer), 215–239.

Berendsen, P., Doveton, J. H., and Speczik, S. (1992). Distribution and characteristics of a middle Ordovician oolitic ironstone in northeastern Kansas based on petrographic and petrophysical properties - a laurasian ironstone case-study. *Sediment. Geol.* 76, 207–219. doi:10.1016/0037-0738(92)90084-5

Bergelin, I., Obst, K., Soderlund, U., Larsson, K., and Johansson, L. (2011). Mesozoic rift magmatism in the north sea region: 40Ar/39Ar geochronology of scanian basalts and geochemical constraints. *Int. J. Earth Sci.* 100, 787–804. doi:10.1007/s00531-010-0516-3

Bomou, B., Adatte, T., Tantawy, A. A., Mort, H., Fleitmann, D., Huang, Y., et al. (2013). The expression of the Cenomanian-Turonian oceanic anoxic event in Tibet. *Palaeogeogr. Palaeoclimatol. Palaeoecol.* 369, 466–481. doi:10.1016/j.palaeo.2012.11.011

Burkhalter, R. M. (1995). Ooidal ironstones and ferruginous microbialites – origin and relation to sequence stratigraphy (Aalenian and Bajocian, Swiss Jura Mountains). *Sedimentology* 42, 57–74. doi:10.1111/j.1365-3091.1995.tb01271.x

Curtis, C. D., Coleman, M. L., and Love, L. G. (1986). Pore water evolution during sediment burial from isotopic and mineral chemistry of calcite, dolomite and siderite concretions. *Geochimica Cosmochimica Acta* 50, 2321–2334. doi:10.1016/0016-7037(86)90085-2

Dera, G., Brigaud, B., Monna, F., Laffont, R., Puceat, E., Deconinck, J.-F., et al. (2011). Climatic ups and downs in a disturbed Jurassic world. *Geology* 39, 215–218. doi:10.1130/g31579.1

Donaldson, W. S., Plint, A. G., and Longstaffe, F. J. (1999). Tectonic and eustatic control on deposition and preservation of Upper Cretaceous ooidal ironstone and associated facies: Peace River Arch area, NW Alberta, Canada. *Sedimentology* 46, 1159–1182. doi:10.1046/j.1365-3091.1999.00271.x

Duncan, R. A., Hooper, P. R., Rehacek, J., Marsh, J. S., and Duncan, A. R. (1997). The timing and duration of the Karoo igneous event, southern Gondwana. *J. Geophys. Res.* 102, 18127–18138. doi:10.1029/97jb00972

Dunn, S. K., Pufahl, P. K., Murphy, J. B., and Lokier, S. W. (2021). Middle ordovician upwelling-related ironstone of north wales: Coated grains, ocean chemistry, and biological evolution. *Front. Earth Sci. (Lausanne).* 9. doi:10.3389/feart.2021.669476

Follmi, K. B. (1993). Phosphorus and phosphate-rich sediments, an environmental approach. *Chem. Geol.* 107, 375–378. doi:10.1016/0009-2541(93)90213-3

Follmi, K. B. (2016). Sedimentary condensation. *Earth-Science Rev.* 152, 143–180. doi:10.1016/j.earscirev.2015.11.016

Follmi, K. B. (1996). The phosphorus cycle, phosphogenesis and marine phosphate-rich deposits. *Earth-Science Rev.* 40, 55–124. doi:10.1016/0012-8252(95)00049-6

Garcia-Frank, A., Ureta, S., and Mas, R. (2012). Iron-coated particles from condensed aalenian - bajocian deposits: Evolutionary model (iberian basin, Spain). *J. Sediment. Res.* 82, 953–968. doi:10.2110/jsr.2012.75

Garzanti, E., Haas, R., and Jadoul, F. (1989). Ironstones in the mesozoic passive margin sequence of the Tethys Himalaya (zanskar, northern India): Sedimentology and metamorphism. *Geol. Soc. Lond. Spec. Publ.* 46, 229–244. doi:10.1144/gsl.sp.1989.046.01.20

Garzanti, E. (1993). Himalayan ironstones, superplumes, and the breakup of Gondwana. *Geol.* 21, 105–108. doi:10.1130/0091-7613(1993)021<0105:hisatb>2.3.co;2

Garzanti, E. (1991). Non-carbonate intrabasinal grains in arenites; their recognition, significance, and relationship to eustatic cycles and tectonic setting. *J. Sediment. Res.* 61 (6), 959–975.

Garzanti, E. (1999). Stratigraphy and sedimentary history of the Nepal Tethys Himalaya passive margin. *J. Asian Earth Sci.* 17 (5-6), 805–827. doi:10.1016/s1367-9120(99)00017-6

Glenn, C. R., and Arthur, M. A. (1988). Petrology and major element geochemistry of Peru margin phosphorites and associated diagenetic minerals – authigenesis in modern organic-rich sediments. *Mar. Geol.* 80, 231–267. doi:10.1016/0025-3227(88)90092-8

Glenn, C. R., Follmi, K. B., Riggs, S. R., Baturin, G. N., Grimm, K. A., Trappe, J., et al. (1994). Phosphorus and phosphorites: Sedimentology and environments of formation. *Eclogae Geol. Helvetiae* 87, 747–788.

Grocke, D. R., Price, G. D., Ruffell, A. H., Mutterlose, J., and Baraboshkin, E. (2003). Isotopic evidence for Late Jurassic-Early cretaceous climate change. *Palaeogeogr. Palaeoclimatol. Palaeoecol.* 202, 97–118. doi:10.1016/s0031-0182(03)00631-x

Han, Z., Hu, X., Boudagher-Fadel, M. K., Jenkyns, H. C., and Franceschi, M. (2021). Early Jurassic carbon-isotope perturbations in a shallow-water succession from the Tethys Himalaya, southern hemisphere. *Newsl. Stratigr.* 54 (4), 461–481. doi:10.1127/nos/2021/0650

Han, Z., Hu, X., He, T., Newton, R. J., Jenkyns, H. C., Jamieson, R. A., et al. (2022). Early Jurassic long-term oceanic sulfur-cycle perturbations in the Tibetan Himalaya. *Earth Planet. Sci. Lett.* 578, 117261. doi:10.1016/j.epsl.2021.117261

Han, Z., Hu, X., Li, J., and Garzanti, E. (2016). Jurassic carbonate microfacies and relative sea-level changes in the Tethys Himalaya (southern Tibet). *Palaeogeogr. Palaeoclimatol. Palaeoecol.* 456, 1–20. doi:10.1016/j.palaeo.2016.05.012

Handoh, I. C., Bigg, G. R., and Jones, E. J. W. (2003). Evolution of upwelling in the atlantic ocean basin. *Palaeogeogr. Palaeoclimatol. Palaeoecol.* 202, 31–58. doi:10.1016/s0031-0182(03)00571-6

Heggie, D. T., Skyring, G. W., O'Brien, G., Reimers, C., Herczeg, A., Moriarty, D., et al. (1990). Organic carbon cycling and modern phosphorite formation on the east Australian continental margin: An overview. *Geol. Soc. Lond. Spec. Publ.* 52, 87–117. doi:10.1144/gsl.sp.1990.052.01.07

Hornibrook, E. R. C., and Longstaffe, F. J. (1996). Berthierine from the lower cretaceous Clearwater formation, Alberta, Canada. *Clays Clay Minerals* 44, 1–21. doi:10.1346/ccmn.1996.0440101

Ifrim, C., Goetz, S., and Stinnesbeck, W. (2011). Fluctuations of the oxygen minimum zone at the end of Oceanic Anoxic Event 2 reflected by benthic and planktic fossils. *Geology* 39, 1043–1046. doi:10.1130/g32161.1

Jacobs, D. K., and Lindberg, D. R. (1998). Oxygen and evolutionary patterns in the sea: Onshore/offshore trends and recent recruitment of deep-sea faunas. *Proc. Natl. Acad. Sci. U. S. A.* 95, 9396–9401. doi:10.1073/pnas.95.16.9396

Jadoul, F., Berra, F., and Garzanti, E. (1998). The Tethys himalayan passive margin from late triassic to early cretaceous (South Tibet). *J. Asian Earth Sci.* 16, 173–194. doi:10.1016/s0743-9547(98)00013-0

Jarvis, I., Burnett, W. C., Nathan, Y., Almbaydin, F. S. M., Attia, A. K. M., Castro, L. N., et al. (1994). Phosphorite geochemistry: Stateof-the-art and environmental concerns. *Eclogae Geol. Helv.* 87, 643–700.

Jenkyns, H. C. (2010). Geochemistry of oceanic anoxic events. *Geochem. Geophys. Geosyst.* 11. doi:10.1029/2009gc002788

Khadkikar, A. S. (1996). Breakup of gondwanaland and the jurassic record of the kachchh basin, Gujarat, Western India. *Curr. Sci.* 70, 1093–1096.

Kimberley, M. M. (1994). Debate about ironstone – has solute supply been surficial weathering, hydrothermal convection, or exhalation of deep fluids. *Terra nova.* 6, 116–132. doi:10.1111/j.1365-3121.1994.tb00645.x

Knight, K. B., Nomade, S., Renne, P. R., Marzoli, A., Bertrand, H., and Youbi, N. (2004). The central atlantic magmatic province at the triassic–jurassic boundary: Paleomagnetic and 40Ar/39Ar evidence from Morocco for brief, episodic volcanism. *Earth Planet. Sci. Lett.* 228, 143–160. doi:10.1016/j.epsl.2004.09.022

Krajewski, K. P., Lesniak, P. M., Lacka, B., and Zawidzki, P. (2000). Origin of phosphatic stromatolites in the upper cretaceous condensed sequence of the polish jura chain. *Sediment. Geol.* 136, 89–112. doi:10.1016/s0037-0738(00)00089-0

Krajewski, K. P., Vancappellen, P., Trichet, J., Kuhn, O., Lucas, J., Martinalgarra, A., et al. (1994). Biological processes and apatite formation in sedimentary environments. *Eclogae Geol. Helvetiae* 87, 701–745.

Larson, R. L., and Erba, E. (1999). Onset of the mid-Cretaceous greenhouse in the Barremian-Aptian: Igneous events and the biological, sedimentary, and geochemical responses. *Paleoceanography* 14, 663–678. doi:10.1029/1999pa900040

Larson, R. L. (1991). Geological consequences of superplumes. *Geol.* 19 (10), 963–966. doi:10.1130/0091-7613(1991)019<0963:gcos>2.3.co;2

Li, X. C., and Grant-Mackie, J. A. (1993). Jurassic sedimentary cycles and eustatic sea-level changes in southern Tibet. *Palaeogeogr. Palaeoclimatol. Palaeoecol.* 101, 27–48. doi:10.1016/0031-0182(93)90150-h

Li, X. H., Jenkyns, H. C., Wang, C. S., Hu, X. M., Chen, X., Wev, Y., et al. (2006). Upper Cretaceous carbon- and oxygen-isotope stratigraphy of hemipelagic carbonate facies from southern Tibet, China. *J. Geol. Soc. Lond.* 163, 375–382. doi:10.1144/0016-764905-046

Li, X. H., and Wang, C. S. (2005). Reinterpretation of jurassic strata of the main himalayan ridge belt, northern Nyalam, South Tibet. *Geol. Bull. China* 12, 1121–1126. (in Chinese with English abatract).

Liu, B. J., Yu, G. M., Wang, C. S., and Lan, B. L. (1983). Jurassic sedimentary environment in Qomolangma region. *Acta Sedimentol. Sin.* 1, 2–14. (in Chinese with English abstract).

Liu, G. H., and Einsele, G. (1994). Sedimentary history of the tethyan basin in the Tibetan himalayas. *Geol. Rundsch.* 83, 32–61. doi:10.1007/BF0021189

McGregor, F., Ramanaidou, E. R., and Wells, M. (2009). *Phanerozoic ooidal ironstone deposits - generation of potential exploration targets*. Perth, AUSTRALIA: Iron Ore Conference 2009, 129–133.

Mucke, A., and Farshad, F. (2005). Whole-rock and mineralogical composition of Phanerozoic ooidal ironstones: Comparison and differentiation of types and subtypes. *Ore Geol. Rev.* 26, 227–262. doi:10.1016/j.oregeorev.2004.08.001

Nelson, G. J., Pufahl, P. K., and Hiatt, E. E. (2010). Paleoceanographic constraints on precambrian phosphorite accumulation, baraga group, Michigan, USA. *Sediment. Geol.* 226, 9–21. doi:10.1016/j.sedgeo.2010.02.001

Pankhurst, R. J., Leat, P. T., Sruoga, P., Rapela, C. W., Marquez, M., Storey, B. C., et al. (1998). The chon aike province of Patagonia and related rocks in west Antarctica: A silicic large igneous province. *J. Volcanol. Geotherm. Res.* 81, 113–136. doi:10.1016/s0377-0273(97)00070-x

Parrish, J. T., Droser, M. L., and Bottjer, D. J. (2001). A triassic upwelling zone: The shublik formation, arctic Alaska, USA. *J. Sediment. Res.* 71, 272–285. doi:10.1306/052600710272

Price, G. D., and Grocke, D. R. (2002). Strontium-isotope stratigraphy and oxygen- and carbon-isotope variation during the middle jurassic-early cretaceous of the falkland plateau, south atlantic. *Palaeogeogr. Palaeoclimatol. Palaeoecol.* 183, 209–222. doi:10.1016/s0031-0182(01)00486-2

Rahiminejad, A. H., and Zand-Moghadam, H. (2018). Synsedimentary formation of ooidal ironstone: An example from the Jurassic deposits of SE central Iran. *Ore Geol. Rev.* 95, 238–257. doi:10.1016/j.oregeorev.2018.02.028

Rao, V. P., and Nair, R. R. (1988). Microbial origin of the phosphorites of the Western continental-shelf of India. *Mar. Geol.* 84, 105–110. doi:10.1016/0025-3227(88)90128-4

Reinhard, C. T., Planavsky, N. J., Gill, B. C., Ozaki, K., Robbins, L. J., Lyons, T. W., et al. (2017). Evolution of the global phosphorus cycle. *Nature* 541, 386–389. doi:10.1038/nature20772

Rudmin, M., Banerjee, S., Abdullayev, E., Ruban, A., Filimonenko, E., Lyapina, E., et al. (2020). Ooidal ironstones in the meso-cenozoic sequences in Western siberia: Assessment of formation processes and relationship with regional and global Earth processes. *J. Palaeogeogr.* 9, 1. doi:10.1186/s42501-019-0049-z

Ruttenberg, K. C., and Berner, R. A. (1993). Authigenic apatite formation and burial in sediments from non-upwelling, continental-margin environments. *Geochimica Cosmochimica Acta* 57, 991–1007. doi:10.1016/0016-7037(93)90035-u

Salama, W., El Aref, M., and Gaupp, R. (2012). Mineralogical and geochemical investigations of the middle eocene ironstones, el bahariya depression, western desert, Egypt. *Gondwana Res.* 22, 717–736. doi:10.1016/j.gr.2011.11.011

Scholz, F. (2018). Identifying oxygen minimum zone-type biogeochemical cycling in Earth history using inorganic geochemical proxies. *Earth-Science Rev.* 184, 29–45. doi:10.1016/j.earscirev.2018.08.002

Schulz, H. N., and Schulz, H. D. (2005). Large sulfur bacteria and the formation of phosphorite. *Science* 307, 416–418. doi:10.1126/science.1103096

Sciunnach, D., and Garzanti, E. (2012). Subsidence history of the Tethys Himalaya. *Earth-Science Rev.* 111 (1-2), 179–198. doi:10.1016/j.earscirev.2011.11.007

Scoteses, C. (2014). Atlas of jurassic paleogeographic maps, PALEOMAP atlas for ArcGIS, volume 4, the jurassic and triassic, maps 32-42, mollweide projection. Evanston: Paleomap project. doi:10.13140/2.1.4850.4321

Shi, X. Y., Yin, J. R., and Jia, C. P. (1995). Mesozoic to cenozoic sequence stratigraphy and sealevel changes in the northern himalayas, southern Tibet, China. *Newsl. Stratigr.* 33, 15–61.

Soudry, D., Glenn, C. R., Nathan, Y., Segal, I., and VonderHaar, D. (2006). Evolution of Tethyan phosphogenesis along the northern edges of the Arabian-African shield during the Cretaceous-Eocene as deduced from temporal variations of Ca and Nd isotopes and rates of P accumulation. *Earth-Science Rev.* 78, 27–57. doi:10.1016/j.earscirev.2006.03.005

Soudry, D., and Lewy, Z. (1988). Microbially influenced formation of phosphate nodules and megafossil moulds (Negev, Southern Israel). *Palaeogeogr. Palaeoclimatol. Palaeoecol.* 64, 15–34. doi:10.1016/0031-0182(88)90139-3

Sturesson, U., Heikoop, J. M., and Risk, M. J. (2000). Modern and Palaeozoic iron ooids - a similar volcanic origin. *Sediment. Geol.* 136, 137–146. doi:10.1016/s0037-0738(00)00091-9

Sturesson, U. (2003). Lower Palaeozoic iron oolites and volcanism from a Baltoscandian perspective. *Sediment. Geol.* 159, 241–256. doi:10.1016/s0037-0738(02)00330-5

Sturesson, U. (1992). Volcanic ash – The source material for ordovician chamosite ooids in Sweden. *J. Sediment. Petrology* 62, 1084–1094.

Surlyk, F. (1991). Sequence stratigraphy of the Jurassic lowermost Cretaceous of east Greenland. *Aapg Bull.* 75, 1468–1488.

Tang, D., Shi, X., Ma, J., Jiang, G., Zhou, X., and Shi, Q. (2017). Formation of shallow-water glaucony in weakly oxygenated Precambrian ocean: An example from the Mesoproterozoic Tieling Formation in North China. *Precambrian Res.* 294, 214–229. doi:10.1016/j.precamres.2017.03.026

Taylor, K. G., and Macquaker, J. H. S. (2011). Iron minerals in marine sediments record chemical environments. *Elements* 7, 113–118. doi:10.2113/gselements.7.2.113

Taylor, S. R., and Mclennan, S. M. (1985). The continental crust: Its composition and evolution. *J. Geol.* 94, 57–72.

Vancappellen, P., and Berner, R. A. (1991). Fluorapatite crystal-growth from modified seawater solutions. *Geochimica Cosmochimica Acta* 55, 1219–1234. doi:10.1016/0016-7037(91)90302-l

Vanhouten, F. B. (1985). Oolitic ironstones and contrasting Ordovician and Jurassic paleogeography. *Geol.* 13, 722–724. doi:10.1130/0091-7613(1985)13<722:oiacoa>2.0.co;2

Vanhouten, F. B., and Purucker, M. E. (1984). Glauconitic peloids and chamositic ooids – favorable factors, constraints, and problems. *Earth-Science Rev.* 20, 211–243. doi:10.1016/0012-8252(84)90002-3

Vanhouten, F. B. (1992). Review of Cenozoic ooidal ironstones. *Sediment. Geol.* 78, 101–110. doi:10.1016/0037-0738(92)90115-8

Wang, C. S., Li, X. H., Hu, X. M., Wan, X. Q., Yin, J. R., Huang, Y. J., et al. (2005). *Tethyan himalayan sedimentary Geology and continental paleoceanography*. Beijing: Geological Publishing House, 373. in Chinese).

Wang, G. X., and Chen, J. Y. (1984). A study on X-ray powder analysis of Fe-Mg-Mn isomorphous substitution in siderite. *Acta Mineral. Sin.* 02, 59–65. (in Chinese with English abstract).

Wigley, R., and Compton, J. S. (2007). Oligocene to holocene glauconite-phosphorite grains from the head of the cape canyon on the Western margin of south Africa. *Deep Sea Res. Part II Top. Stud. Oceanogr.* 54, 1375–1395. doi:10.1016/j.dsr2.2007.04.004

Wignall, P. B., and Hallam, A. (1989). *Biofacies, stratigraphic distribution and depositional models of British onshore Jurassic black shales*. London, England: Meeting on Modern and Ancient Continental Shelf Anoxia, 291–309.

Yin, J. R., Callomon, J. H., and Enay, R. (2000). A hiatus of 8 My duration in the middle jurassic with ammonite succession in tethyan Himalaya (South Tibet). *Geobios* 33, 201–210. doi:10.1016/s0016-6995(00)80017-0

Yin, J. R. (2010). *Jurassic ammonites of Tibet*. Beijing: Geological Publishing House, 227–235. in Chinese with English abstract).

Young, T. P. (1989). *Phanerozoic ironstones: an introduction and review*. London: Geological Society, Special Publications, 46. ix-xxv.

Young, T. P. (1992). Ooidal ironstones from ordovician gondwana – A review. *Palaeogeogr. Palaeoclimatol. Palaeoecol.* 99, 321–347. doi:10.1016/0031-0182(92)90021-v

Zhu, D., Pan, G., Mo, X., Liao, Z., Jiang, X., and Wang, L. (2004). Permian to cretaceous volcanic activities in the central segment of the tethyan himalayas (I): Distribution characteristics and significance. *Geol. Bull. China* 23, 645–654.